JOURNAL OF
Materials
CHEMISTRY

Structural–magnetic phase diagram of Mo-substituted $CaMnO_3$: consequences for thermoelectric power properties

A. Maignan,*[a] C. Martin,[a] C. Autret,[a] M. Hervieu,[a] B. Raveau[a] and J. Hejtmanek[b]

[a]*Laboratoire CRISMAT, UMR 6508, ISMRA et Université de Caen, 6 Bd du Maréchal Juin, 14050 Caen Cedex, France. E-mail: antoine.maignan@ismra.fr; Fax: 33 2 31 95 16 00; Tel: 33 2 31 45 26 34*

[b]*Institute of Physics of ASCR, Cukrovarnicka 10, 16200 Praha 6, Czech Republic*

Received 14th January 2002, Accepted 27th February 2002
First published as an Advance Article on the web 10th April 2002

The substitution of molybdenum for manganese has been studied in the $CaMn_{1-x}Mo_xO_3$ series for $0 \leqslant x \leqslant 0.15$. We establish a structural and magnetic diagram combining electron microscopy, neutron diffraction and magnetic susceptibility measurements. Four regions have been evidenced *versus* composition (x) and temperature. The transport properties and thermoelectric power have been analyzed on the basis of this diagram. The structural transition temperature, linked either to a monoclinic deformation characteristic for antiferromagnetism (AFM) with a C-type orbital polarization ($0.07 \leqslant x \leqslant 0.12$) or associated with ordered stripes ($x > 0.12$), significantly increases with x. The fact that these orders develop at high temperatures (exceeding 300 K) is determined by two favourable parameters: the A-site cationic mismatch is zero and the magnetic order, linked with the orbital one, is not confronted with the magnetic sub-lattice of rare-earth ion. The great analogy of these materials with the Mn^{4+}-rich manganites $Sm_{1-x}Ca_xMnO_3$ is discussed, referring to the injection of electrons in the $CaMn^{IV}O_3$ matrix.

Introduction

The substitution of trivalent lanthanides for calcium in the G-type antiferromagnetic insulator $CaMnO_3$ allows original magnetic and transport properties to be generated as shown for the $Ln_{1-x}Ca_xMnO_3$ perovskites.[1–4] In these series, besides the charge-ordered compositions,[5–11] the Mn^{4+} rich region ($x \approx 0.9$), which corresponds to the injection of electrons at low concentration in the Mn^{4+} matrix, is of great interest since it promotes a metallic-like resistivity,[12] and shows magnetic phase separation below T_N ($T_N \approx T_C \approx 110$ K; T_C = Curie temperature, T_N = Néel temperature), involving a G-type antiferromagnetic (AFM) phase and a ferromagnetic (FM) phase.[13,14]

Another way to introduce electrons at low concentration in the Mn^{4+} matrix consists of doping the manganese sites of $CaMnO_3$, with cations of higher valency than 4+. The doping of this oxide with hexavalent molybdenum shows indeed the possibility to induce ferromagnetism in the compounds $CaMn_{1-x}Mo_xO_3$ for low x values ($x \leqslant 0.04$),[15] due to the formation of Mn^{3+} species, similarly to the $Ln_{1-x}Ca_xMnO_3$ compounds. However, in contrast to the latter no metallicity is induced due to the d^0 electronic configuration of Mo^{VI} which breaks the conductivity paths. But more surprising is the recent discovery of superstructures as observed in the orbital/charge ordered (OO/CO) samples for higher molybdenum contents ($x > 0.12$) in the $CaMn_{1-x}Mo_xO_3$ oxides.[16] Such a result is indeed in contradiction with the idea that the doping of the Mn-site with foreign cations induces disorder and consequently prevents or destroys charge ordering.

The present study is devoted to the structural, magnetic and transport properties of the molybdenum-doped oxides $CaMn_{1-x}Mo_xO_3$. We establish a structural and magnetic phase diagram of this system for $0 \leqslant x \leqslant 0.15$ and an attempt is made to explain the transport properties and especially the evolution of thermoelectric power *versus* temperature on the basis of this diagram.

Experimental

The synthesis of the $CaMn_{1-x}Mo_xO_3$ samples with $0 \leqslant x \leqslant 0.15$ (for higher x values $CaMoO_4$ appears as secondary phase) has been previously described.[15,16]

For all the samples, the room temperature X-ray patterns were obtained using Cu-Kα radiation and refined with the Fullprof program. Three samples $x = 0.10$, 0.12 and 0.14 were studied by neutron powder diffraction (NPD), *versus* temperature from 1.5 to 300 K, in LLB-Saclay (France) on the G41 diffractometer ($\lambda = 2.4266$ Å).

The samples for electron microscopy were prepared by dispersing the crystallites in alcohol. The particles were deposited on a holey carbon film supported by a Cu grid. The electron diffraction (ED) study was carried out at room temperature (RT) and down to 92 K using JEOL 200CX and JEOL 2010 electron microscopes.

The ac magnetic susceptibility (ac-χ) and dc magnetization data were collected with a SQUID magnetometer [$h_{ac} = 3$ Oe, $f = 1$–10^3 Hz; $0 < h_{dc} \leqslant 5$ T; 5 K $\leqslant T \leqslant$ 400 K]. Resistivity (5 K $\leqslant T \leqslant$ 400 K), TEP and thermal conductivity (5 K $\leqslant T \leqslant$ 320 K) were all measured in the same Physical Properties Measurements System (PPMS, Quantum Design), which also allows magnetic field scans in the range 0–9 T. The resistance was measured with the four-probe technique on 2 × 2 × 10 mm bars. For the thermopower measurements, the four points steady-state method, with separated measuring and power contacts, was used to eliminate the thermal resistances between the sink and the heater, respectively. The rectangular shaped sample was affixed on the cell mounted on the PPMS puck, and the miniature resistor heater (charged using a pair of 72 µm chromel wires) was stuked by GE varnish on the end of the sample. The temperature gradient and voltage drop was monitored using two separated differential chromel–constantan thermocouples (72 µm in diameter) which were affixed to the sample using indium solder. With respect to the sensibility of used E-type thermocouples, a temperature difference across

DOI: 10.1039/b200495j

the sample $\Delta(T)/K = 0.5 + 0.005T$ was applied. The influence of magnetic field on the measured temperature gradient and the thermopower of chromel was calibrated using reference nonmagnetic (high temperatures) and superconducting (low temperatures) samples. The significant impact of the magnetic field on the measured thermal gradient and thermovoltage only for temperatures below 20 K was observed and the corresponding corrections made.

Results and discussion

Structural phase diagram

The structural and magnetic phase diagram of the $CaMn_{1-x}Mo_xO_3$ manganites for $0 \leqslant x \leqslant 0.15$ (Fig. 1) was obtained by combining electron microscopy, neutron diffraction and magnetic susceptibility measurements.

From the structural viewpoint (*i.e.*, referring to the observed space groups), four regions can be distinguished in this diagram.

The first one corresponds to the well known *Pnma* structure, characterized by the cell parameters "$a_p\sqrt{2} \times 2a_p \times a_p\sqrt{2}$". It is observed, whatever the temperature for $0 \leqslant x \leqslant 0.06$, and above a line labelled T_{OO} (orbital ordering temperature) for $0.06 < x \leqslant 0.15$. This structure can easily be identified from its [010] electron diffraction pattern as shown for the sample $x = 0.10$ observed at room temperature (lower panel (a) in Fig. 1). It is confirmed by the indexation of the corresponding neutron powder diffraction patterns (Fig. 2).

The second region, labelled $P2_1/m$, corresponds to a monoclinic distortion of the structure. The cell parameters are $a_p\sqrt{2} \times 2a_p \times a_p\sqrt{2}$, similar to those of the previous *Pnma* region, but $\beta > 90°$. The [010] ED patterns systematically exhibit a splitting of the reflections, due to twinning phenomena, as illustrated for $x = 0.10$ registered at 92 K (lower pattern (b) in Fig. 1). This monoclinic distortion is also confirmed by the indexation of the corresponding NPD patterns (Fig. 2). This second structural region extends from $x = 0.07$ to $x = 0.12$ below the T_{OO} line.

The third region, labelled OO/CO, is characterized by ED patterns exhibiting extra satellites in incommensurate positions suggesting orbital/charge ordering. A typical [010] ED pattern is shown for $x = 0.14$ registered at 92 K in Fig. 2c, showing a modulation vector parallel to a^* and of amplitude qa^*, with $q \approx 0.23$. A detailed electron microscopy and NPD study of the charge-ordering phenomena in these oxides will be published elsewhere.[17] This third, OO/CO region extends from $x = 0.13$ to 0.15, and is limited in temperature by the appearance of a fourth region (hatched region on Fig. 1), which corresponds to a transition zone between the two structures (with and without CO), which coexist in the form of strained domains within the same crystal.

This fourth region is illustrated by the ED study of the evolution of the modulation of the structure, characterized by

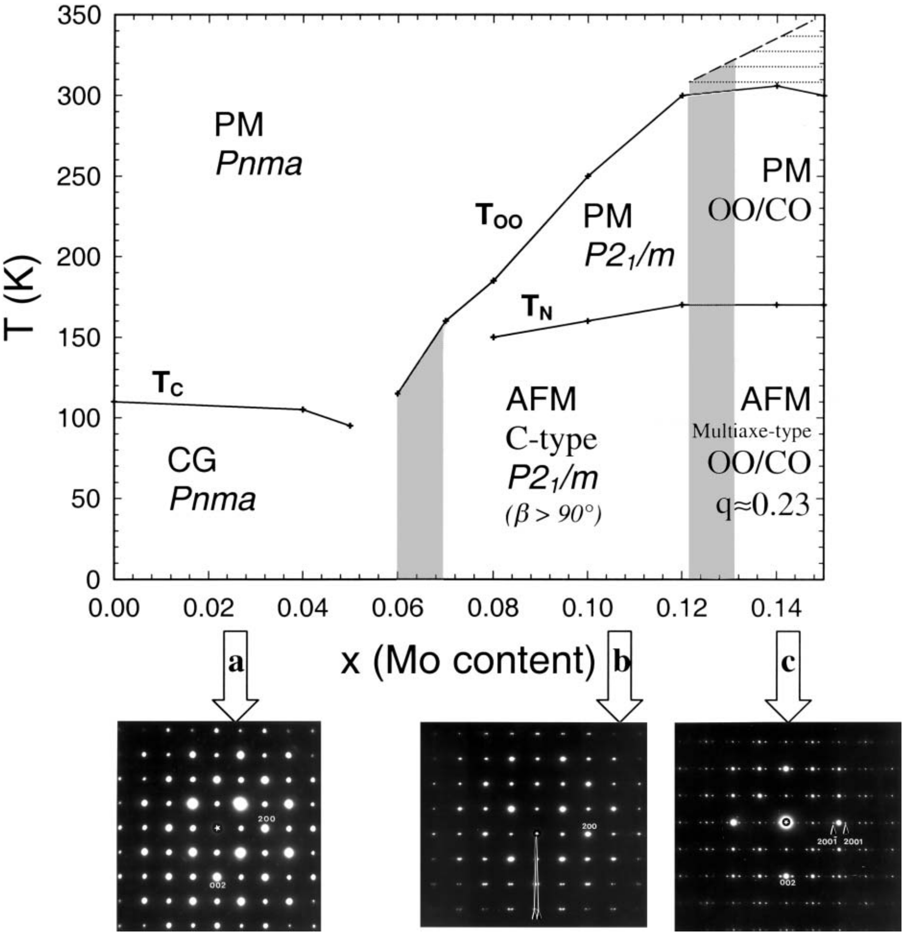

Fig. 1 Structural phase diagram of the manganites $CaMn_{1-x}Mo_xO_3$ ($0 \leqslant x \leqslant 0.15$), built up from ED, NPD and magnetic susceptibility data. (CG = cluster glass; T_C, T_N and T_{OO} = Curie, Néel and orbital ordering temperatures, respectively). The hatched area corresponds to an intermediate zone with a mixture of structures with and without CO. The grey regions are only drawn to show the transition areas from *Pnma* to $P2_1/m$ and then towards CO. [010] ED patterns characteristic of the three structures are also given (lower panels): (a) *Pnma*-type (observed whatever T for $0 \leqslant x \leqslant 0.06$). The forbidden $h00$, $h = 2n$ and $00l$, $l = 2n$ reflections arise from double diffraction phenomena. (b) Monoclinic $P2_1/m$ structure characteristic of the C-type AFM phase (below T_{OO} for $0.06 < x < 0.15$). The white lines form a 2ε angle and are drawn to show the monoclinic distortion. (c) [010] ED pattern characteristic of the charge-ordered phase with an incommensurate modulated structure (the reflections are indexed using four indices $h0lm$).

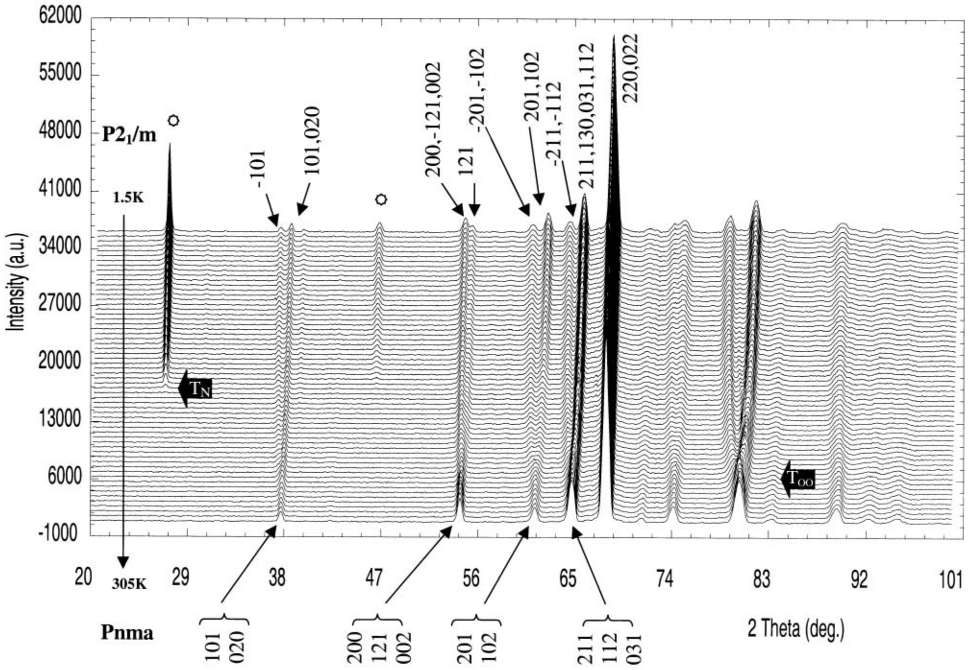

Fig. 2 Neutron powder diffraction patterns of $CaMn_{0.9}Mo_{0.1}O_3$ ($\lambda = 2.4266$ Å) collected from 1.5 to 305 K. The transition temperatures (T_{OO} and T_N) are shown with the black arrows, some indexations are given for the crystalline structure and the stars are for the magnetic peaks characteristic of C-type.

the amplitude of the modulation vector q, *versus* temperature for the $x = 0.14$ sample. The sample was warmed from 92 K up to 350 K by steps of 5 K waiting for the temperature stabilization between each step. The $q(T)$ curve is given in Fig. 3 and illustrated with the ED patterns recorded at room temperature (inset of Fig. 3). The q value does not significantly evolve up to $\approx$170 K ($q = 0.23$) and, from this temperature, it slightly decreases down to reach 0.215 at $\approx$250 K. At higher temperature, q keeps on decreasing but a change is observed in the satellites, which become slightly streaky and cross-shaped. At room temperature (inset of Fig. 3), the crossed shape of the satellites is still observed, and nodes corresponding to $q \approx 0.17$ are detected (see the black arrows). This effect is observed up to 320 K, the streaky aspect increasing whereas the intensity of the satellites strongly decreases and they are no longer detectable at $\sim$335 K.

Finally it must be noticed that the grey area on Fig. 1 corresponds to transition zones between the *Pnma*, *P*2₁/*m* and their superstructures; more compositions would be necessary to determine the exact composition where the structural transitions appear, and moreover it is also possible that different phases coexist in small x ranges.

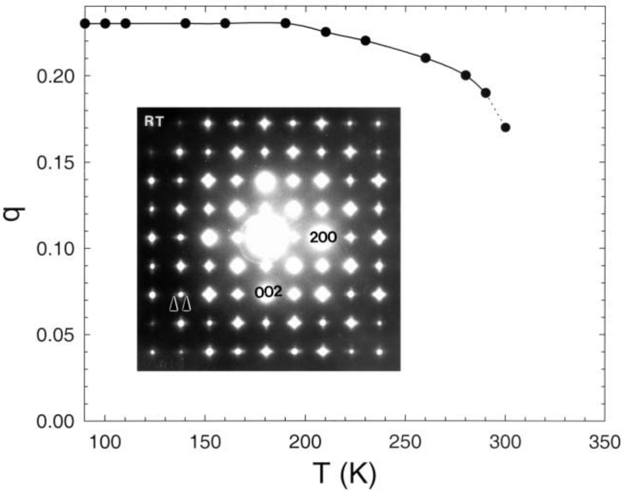

Fig. 3 $x = 0.14$: evolution of the q values *vs.* T (temperature increasing from 92 K to 300 K). The lines are only a guide to the eye. The dotted line symbolizes the fact that above 290 K the satellites are diffuse. Inset: [010] ED pattern registered at RT for the $x = 0.14$ compound. The black arrow indicates two satellites, $\bar{3}021$ and $\bar{3}02\bar{1}$ ($q \approx 0.17$).

Magnetic phase diagram

The fact that the structural transition (*vs T*) from the *Pnma* to the *P*2₁/*m* structure can be described as orbital ordering (OO) is corroborated by the $\chi'(T)$ measurements of several samples (inset of Fig. 4) which exhibit a peak at 160 K, 260 K and 300 K for $x = 0.07$, 0.10 and 0.12, respectively, *i.e.*, at temperatures coinciding exactly with the T_{OO} line deduced from the structural measurements (Fig. 1). By further cooling, the $\chi'(T)$ curves of the samples corresponding to $0.08 \leqslant x \leqslant 0.12$, exhibit a shoulder at $T_N \approx 160$ K (see the $x = 0.10$ and $x = 0.12$ curves in the inset of Fig. 4) which characterizes a transition from the paramagnetic (PM) to the antiferromagnetic state. Thus, the *P*2₁/*m* region of the diagram (Fig. 1) is

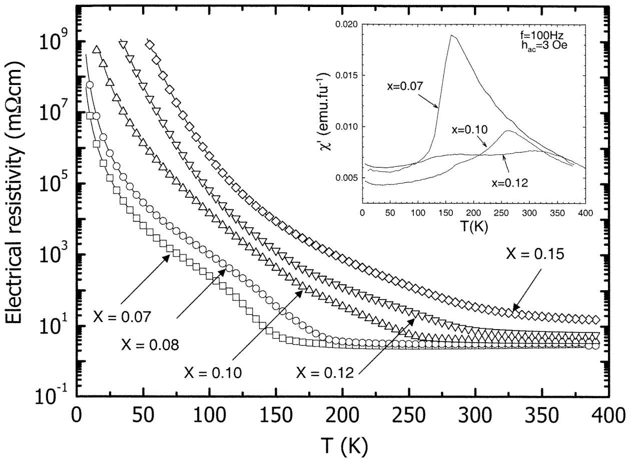

Fig. 4 *T*-dependent resistivity (ρ) of several $CaMn_{1-x}Mo_xO_3$ samples. Inset: *T*-dependence of the real part of the magnetic susceptibility (χ'). x values are labelled in the graphs.

subdivided into two regions, a $P2_1/m$ PM region above T_N and a $P2_1/m$ AFM one below this temperature. The corresponding NPD patterns confirm also this PM to AFM transition as shown for $x = 0.10$, which starts developing magnetic peaks below $T_N = 160$ K (Fig. 2). Moreover the indexation of these peaks (labelled with stars on the patterns) shows that this AFM structure belongs to the C-type, *i.e.*, consists of FM files antiferromagnetically coupled, the d_z^2 orbitals being polarized along the files.[1,2] For $0.13 \leqslant x \leqslant 0.15$, the OO/CO region is also divided into two regions, PM and AFM at high and low temperatures, respectively. The T_N determined from the NPD data is also close to 160 K. However, the structure of the AFM phase is of a different nature, showing a supercell "$4a_p\sqrt{2} \times 2a_p \times 2a_p\sqrt{2}$" in agreement with the ED results ($q \approx 0.23$). The AFM structure, close to that reported for $Pr_{0.25}Ca_{0.75}MnO_3$,[18] will be studied separately.[17]

Finally it is worth pointing out that in the *Pnma* region for $0 \leqslant x \leqslant 0.06$, a transition from the PM to the weak FM state was previously observed at decreasing temperature,[15] with a T_C ranging from 90 K to 110 K (Fig. 1).

Thermoelectric power (TEP) and thermal conductivity

The previous study of the $CaMn_{1-x}Mo_xO_3$ series[15] for low doping levels ($x \leqslant 0.06$) showed that the $\rho(T)$ evolution is closely connected to the magnetic behavior, since for these compositions, it was shown that the PM to weak FM transition coincides with a metal (or semi-metal) to insulator transition at decreasing temperature. For higher doping levels, a similar resistive transition is observed (Fig. 4), at least up to $x = 0.12$, T_{M-I} increasing with the Mo content. The low absolute value of the resistivity observed at room temperature (2–3 mΩ cm), anticipates the minor role of grain boundaries in transport properties. Consequently, a relevant resistivity analysis can be made to characterize more clearly the M–I discontinuities. The temperature dependence of the local activation energy, defined as

$$W_{\mathrm{local}} = \frac{\mathrm{d}(\ln(\rho))}{\mathrm{d}(1/T)}$$

is then plotted on Fig. 5. For $x = 0.07$, we observe a single peak of W_{local} with a maximum at ~130 K accompanied by a minor shoulder at ~150 K. For higher contents, *i.e.*, for $0.07 < x \leqslant 0.15$, a very pronounced double peak feature of W_{local} is observed. By comparing the temperature dependence of W_{local} with the magnetic susceptibility and structural data for the $x = 0.10$ sample we observe the temperature coincidence between the low temperature peak of W_{local} and a shoulder in the real part of the magnetic susceptibility $\chi'(T)$ (onset of long range magnetic order T_N) and, simultaneouly, between the dominant $\chi'(T)$ peak (onset of OO/CO ordering T_{OO}) and the inflection point of the edge of the high temperature W_{local} peak.

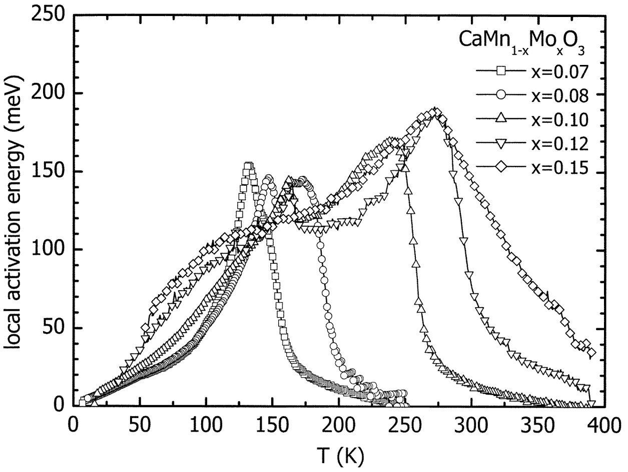

Fig. 5 Local activation energy as a function of T for $CaMn_{1-x}Mo_xO_3$ compounds.

To further correlate the transport properties to the structural aspects, thermoelectric power measurements were carried out for the $CaMn_{1-x}Mo_xO_3$ series and the results are shown in Fig. 6. Similarly to the resistivity and W_{local} temperature dependence, we can distinguish the different characteristic temperatures. For the $x = 0.07$, 0.08 and 0.10 samples the linear temperature dependence in the paramagnetic state, typical for metals, fits well with the small and metallic-like resistivity observed in Fig. 4.The negative absolute value agrees with an electron-like conduction in the Mn e_g –O 2p σ^* band. The high absolute value, unusual in a first approximation classical metallic picture, is likely linked with the high negative offset of the linear temperature dependence. Using the classical Mott formula for thermopower:

$$S = \frac{\pi^2 k_B^2 T}{3|e|} \frac{\partial \ln \sigma(E)}{\partial E}\bigg|_{E=E_F}$$

and supposing $\sigma = n(E)e\mu(E)$, we can link the negative intercept of thermopower linear temperature dependence in disordered paramagnetic state with energy dependent mobility

$$\frac{\partial \ln \mu(E)}{\partial E}\bigg|_{E=E_F}$$

This hypothesis is reinforced by the fact that the thermally excited electrons should have a higher mobility than at E_F due of the possibility of the ordering instability. Indeed this quasi-metallic behaviour is broken below $T_{\mathrm{crit}} \approx 200$ K and ≈ 250 K for $x = 0.08$ and $x = 0.10$, respectively, temperatures from which the thermopower values start to decrease. This thermopower decrease is consequently interpreted considering the structural magnetic phase diagram (Fig. 1). The latter shows the occurrence of a monoclinic distortion linked with the C-type AFM below ~260 K for $CaMn_{0.9}Mo_{0.1}O_3$, connected with the onset of $3d_{z^2-r^2}$ orbital polarization.

The metallic-like "conductivity" is at T_{OO} transformed into an insulating one with a hopping mechanism of charge-carrier transport. In that case, the thermopower is determined by a configurational entropy of hopping carriers according to

$$S = \frac{k_B}{|e|} \ln\left(\beta \frac{1-c}{c}\right)$$

where β accounts for additional spin and orbital degrees of freedom and $c = n/N$ with n being the number of hopping electrons and N the number of available sites.[19] So, below T_{crit}, the e_g electrons start to be "trapped" for a significantly longer time, thus gradually creating "quasistatic" Mn^{3+} ions, so that the effective concentration of relatively free electrons participating in carrier transport decreases.

Nonetheless when the temperature is further lowered, a more complicated behaviour is observed. We show this evolution for $CaMn_{0.9}Mo_{0.1}O_3$ (Fig. 6) where below 160 K, which is the Néel temperature of the C-type antiferromagnetic order, the thermopower goes through a minimum as T decreases. On further cooling at ~75 K a transition from n-type to p-type conductivity is observed and below the positive maximum culminating at ~30–40 μV K^{-1} (~50 K) the thermopower tends toward zero at 4.2 K.

The gradual change towards a hole-like behaviour at low temperatures was already observed in the electron-doped $Sm_{0.2}Ca_{0.8}MnO_3$ and $Pr_{0.15}Sr_{0.85}MnO_3$ manganites, as demonstrated for comparison Fig. 6. These compounds exhibit the same C-type antiferromagnetic arrangement with ferromagnetic Mn $3d_{z^2-r^2}$ chains, which are interlinked antiferromagnetically

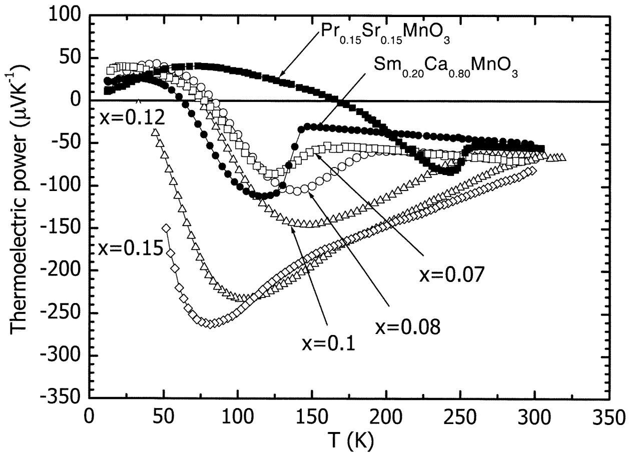

Fig. 6 T-dependent thermopower of $CaMn_{1-x}Mo_xO_3$ (x = 0.07, 0.08, 0.1, 0.12 and 0.15), $Sm_{0.2}Ca_{0.8}MnO_3$ and $Pr_{0.15}Sr_{0.85}MnO_3$.

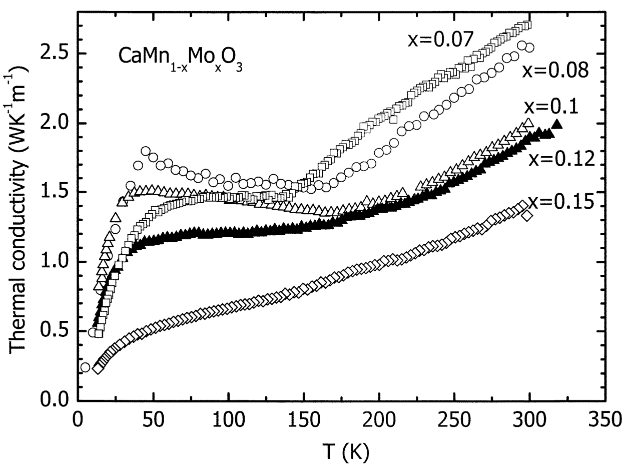

Fig. 7 T-dependence of the thermal conductivity for the series $CaMn_{1-x}Mo_xO_3$.

below T_N = 140 and 250 K, respectively.[20–22] It was attempted to explain the positive low temperature thermopower of C-type AFM in coherence with the structural data as a product of: (i) the experimentally observed elongation of the MnO_6 octahedra, implying orbital ordering (OO) of Mn $3d_{z^2-r^2}$ orbitals in ferromagnetic chains, (ii) the absence of long-range charge ordering and (iii) the chemical composition determining the e_g electron concentration. Following this picture a substantially higher electron density in $3d_{z^2-r^2}$ orbitals, imposed by elongation of the MnO_6 octahedra, than that provided by chemical composition results in a positive thermopower of charge carriers (hole-like character) hopping along ferromagnetic chains.

By adopting this scenario we note that the dimensionality crossover from 3D in the orbital disordered pseudocubic structure of the paramagnetic state to 1D with C-type $3d_{z^2-r^2}$ orbital polarization is likely completed only when the long range antiferromagnetic order is stabilized, since the thermopower starts to increase only below T_N from NPD. Such an orbital ferroelectric polarization sets along the 1D chains where the carrier transport does not need the spin reversal while, obviously, the antiferromagnetic coupling between chains is more difficult to overcome. In this context, one can speculate that oxygen "holes" resulting from electron density transferred from oxygen to manganese are the "hole-like" charge carriers hopping along the FM chains detected by the thermopower measurements.

Accordingly, it should be emphasized that the low temperature resistivity fit, checked for the $x = 0.08$ sample, was the best supposing the 1D variable range hopping (VRH), the attempt to impose higher dimensionality provides both a significantly worst fit and unreasonable parameters. Nevertheless an admixture of $3d_{z^2-r^2}$ to dominating $3d_{z^2-r^2}$ orbital polarization cannot be ruled out. In this way, let us note that the 1D conduction being, in principle, very unstable is easily disrupted and consequently a VRH behavior with thermally activated hopping in higher dimension is observed.

For the $x = 0.12$ sample, the thermopower declines below ~300 K and when the Mo content is further increased up to $x = 0.15$ only a smooth decrease commencing well above 300 K is observed at room temperature. For these samples with a high Mo content the charge carrier localization, responsible for the increase of the absolute value of thermopower with decreasing temperature is simultaneously supported by the resistivity measurements and the structural–magnetic phase diagram (Fig. 1). This last fact confirms the existence of charge ordering, which persists at room temperature.

On the other hand, the $x = 0.12$ and 0.15 samples exhibit a different behavior with respect to evolution below the long range magnetic order. Contrary to samples with Mo $\leqslant$ 0.10, where just below T_N the negative thermopower starts to increase, the thermopower of Mo-rich samples displays an increasing decay at 170 and 150 K, respectively. When the temperature is substantially decreased, the minimum of ~250 μV K^{-1} is reached and, finally, the thermopower increases below 100 and 80 K, respectively. Note that our structural–magnetic phase diagram cannot easily explain this different behavior.

To complete the picture of Mo substitution in $CaMnO_3$, we complement the transport and magnetic data by thermal conductivity temperature dependence (Fig. 7). Similarly to other manganites, the absolute value of thermal conductivity is very low and is similar to glassy materials. The expected increase with decreasing temperature, typical for crystalline solids, is not detected, and, on the contrary, the thermal conductivity decreases with decreasing temperature. This effect can be ascribed to the disorder due to the chemical substitution and to the local lattice distortions linked with quasi-static Mn^{3+} ions. The absolute values of electrical resistivity, linked with the electronic component of thermal conductivity by the Wiedemann–Franz law, indicate that the measured thermal conductivity is dominated by phonon contribution. The observed anomalies, if any, are thus linked with the lattice effects. The thermal conductivity of $x = 0.07$, 0.08 and 0.10 exhibits a clear increase at 140, 155 and 170 K, respectively, *i.e.*, at temperatures T_N, very close to T_N. For higher Mo doping the smooth decrease with decreasing temperature is preserved from 300 K to low temperature. The comparison of the anomalies observed for $x = 0.07$, 0.08 and 0.1 samples with magnetic, structural and thermopower shows that, as soon as the long range AFM magnetic order is stabilized, the phonons become less scattered. However, the absence of anomaly at OO/CO temperature, observed for the whole composition range, $0.07 \leqslant x \leqslant 0.15$, *i.e.* the formation of Mn^{3+} ions with $3d_{z^2-r^2}$ polarization, detected by other experimental techniques [ED, $\rho(T)$ and $\chi(T)$] at significantly higher temperatures than T_N suggests, that a strong anharmonic dynamics limits the mean free path of phonons and survives down to T_N. Finally let us point out that the absence of the thermal conductivity revival for the $x = 0.12$ and 0.15 samples below T_N likely suggests that the anharmonic dynamics of e_g orbital ordering is even preserved in the AFM structure.

Concluding remarks

This study of the structural–magnetic phase diagram of the manganites $CaMn_{1-x}Mo_xO_3$ shows a great analogy with the behavior of the Mn^{4+}-rich manganites $Ln_{1-x}Ca_xMnO_3$ for

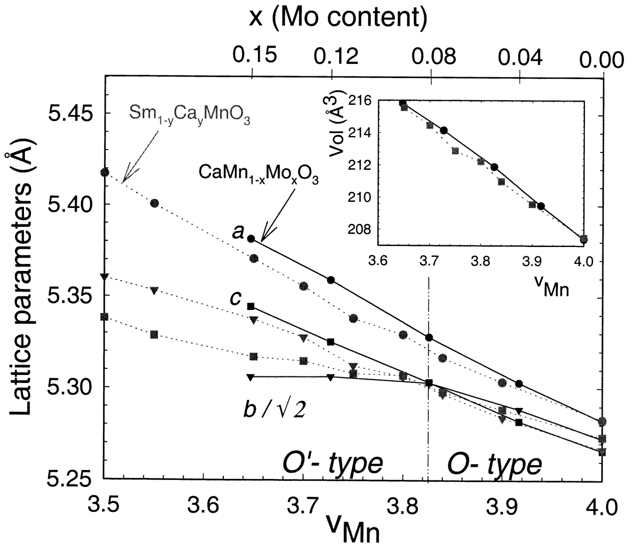

Fig. 8 Evolution of the room temperature lattice parameters *versus* Mn valency (lower x-axis) for the $\mathrm{Sm}_{1-y}\mathrm{Ca}_y\mathrm{MnO}_3$ (grey symbols and dotted line) and $\mathrm{CaMn}_{1-x}\mathrm{Mo}_x\mathrm{O}_3$ (dark symbols and continuous line) series. For the latter, the cell parameters are also given *versus* the Mo content (upper x-axis). The lines are only a guide for the eye. The same conventions are used for the Mn-valency dependence of the cell volume for both systems in the inset.

which besides the cluster glass state observed for low electron doping levels ($x \approx 0.90$), orbital and charge ordering was evidenced in a C-type AFM structure at higher electron concentrations ($0.75 < x < 0.90$) and finally charge ordering for $0.3 < x < 0.75$.[11,12,23] This great similarity is also evidenced by the structural evolution *versus* the Mn valency. In fact, for both series $\mathrm{CaMn}_{1-x}\mathrm{Mo}_x\mathrm{O}_3$ and $\mathrm{Sm}_{1-y}\mathrm{Ca}_y\mathrm{MnO}_3$,[11] as shown in Fig. 8, the lattice expands as x increases or y decreases, in agreement with the Mn^{3+} content increase. To draw this picture, the room temperature X-ray data have been refined in the *Pnma* space group, even for $x \geqslant 0.1$, for which a complex microstructure is observed at RT (as previously shown,)[16] in order to characterize an average cell and the Mn valency (v_{Mn}) is deduced by assuming the $\mathrm{CaMn}^{4+}_{1-3x}\mathrm{Mn}^{3+}_{2x}\mathrm{Mo}^{6+}_{x}\mathrm{O}_3$ formula. This similarity in the structural evolutions demonstrates that the lattice parameters are mainly governed by the Mn valency according to the larger ionic radius of Mn^{3+} than that of Mn^{4+}.[24] In particular, an increase of the orthorhombic distortion, starting from the same Mn valency, around Mn^{3+8} is observed in both series. This point splits the diagram in two parts: the lattice distortion is from O-type ($c \leqslant b/\sqrt{2} < a$) near CaMnO_3 and from O'-type ($b/\sqrt{2} \leqslant c < a$), that is linked to a cooperative Jahn–Teller orbital ordering, towards the richer Mn^{3+} compounds.[4,25] This demonstrates that the injection of electrons in the CaMnO_3 matrix either by substitution on the calcium sites ($\mathrm{Ln}_{1-x}\mathrm{Ca}_x\mathrm{MnO}_3$) or on the manganese sites ($\mathrm{CaMn}_{1-x}\mathrm{Mo}_x\mathrm{O}_3$) leads to very similar background states, generating comparable cluster glass phases, C-type AFM and OO/CO structures. Nevertheless it is remarkable that the manganese site doping induces higher structural transition temperatures (T_{OO}) compared to A-site substitution. This difference may be explained by the fact that in $\mathrm{Ln}_{1-x}\mathrm{Ca}_x\mathrm{MnO}_3$ manganites, the mismatch of the A-site is an important parameter[26] and the magnetic lanthanides (Pr^{3+}, Sm^{3+}) interact with the magnetic manganese array. In contrast in $\mathrm{CaMn}_{1-x}\mathrm{Mo}_x\mathrm{O}_3$ manganites, no mismatch effect has to be taken into account and Mo^{6+}, due to its d^0 configuration, can accommodate various distorted octahedral coordinations, which can be imposed by the Jahn–Teller distorted Mn^{3+} species. Moreover, the presence of such a d^0 cation hinders the possible short-range ferromagnetic correlations which exist above T_{OO} between Mn^{3+} and Mn^{4+} in manganites,[27] favoring in this way orbital ordering. More surprising is the appearance of a superstructure, established at long range, in contradiction with the fact that the introduction of a foreign element on the Mn sites is expected to prevent or destroy ordering.

Acknowledgement

The authors express their gratitude to Dr G. André and Dr F. Bourée for the NPD records and their well-advised help for interpretation of these data.

References

1 J. B. Goodenough, *Phys. Rev.*, 1955, **100**, 564.
2 E. O. Wollan and W. C. Koehler, *Phys. Rev.*, 1955, **100**, 545.
3 A. P. Ramirez, *J Phys.: Condens. Matter*, 1997, **9**, 9171; C. N. R. Rao, A. Arulfaj, A. K. Cheetham and B. Raveau, *J. Phys.: Condens. Matter*, 2000, **12**, R83.
4 Z. Jirak, S. Krupicka, Z. Simsa, M. Dlouha and S. Vratislav, *J. Magn. Magn. Mater.*, 1985, **53**, 153.
5 V. A. Bokov, N. A. Grogoryan and M. F. Bryzhina, *Phys. Status Solidi*, 1967, **20**, 745.
6 H. Chiba, M. Kikuchi, K. Kusaba, Y. Muraoka and Y. Syono, *Solid State Commun.*, 1996, **99**, 499.
7 W. Bao, J. D. Axe, C. H. Chen and S. W. Cheong, *Phys. Rev. Lett.*, 1997, **78**, 543.
8 Y. Murakami, D. Shindo, H. Chiba, M. Kikuchi and Y. Syono, *Phys. Rev. B*, 1997, **55**, 15043.
9 Y. Su, C. H. Du, P. D. Hatton, S. P. Collins and S. W. Cheong, *Phys. Rev. B*, 1999, **59**, 11687.
10 I. O. Troyanchuck, N. V. Samsonenko, H. Szymczak and A. Nabaliek, *J. Solid State Chem.*, 1997, **131**, 144.
11 M. Hervieu, A. Barnabé, C. Martin, A. Maignan, F. Damay and B. Raveau, *Eur. Phys. J. B*, 1999, **8**, 31.
12 A. Maignan, C. Martin, F. Damay and B. Raveau, *Chem. Mater.*, 1998, **10**, 950; A. Maignan, C. Martin, F. Damay, B. Raveau and J. Hejtmanek, *Phys. Rev. B*, 1998, **58**, 2758.
13 C. Martin, A. Maignan, M. Hervieu, B. Raveau, Z. Jirak, M. M. Savosta, A. Kurbakov, V. Trounov, G. André and F. Bourée, *Phys. Rev. B*, 2000, **62**, 6442.
14 M. M. Savosta, P. Novak, M. Marysko, Z. Jirak, J. Hejtmanek, J. Englich, J. Kohout, C. Martin and B. Raveau, *Phys. Rev.*, 2000, **62**, 9532.
15 B. Raveau, Y. Zhao, C. Martin, M. Hervieu and A. Maignan, *J. Solid State Chem.*, 2000, **149**, 203.
16 C. Martin, A. Maignan, M. Hervieu, B. Raveau and J. Hejtmanek, *Phys. Rev. B*, 2001, **63**, 100406(R).
17 C. Autret, C. Martin, M. Hervieu, A. Maignan, Z. Jirak and B. Raveau, to be published.
18 Z. Jirak, C. Martin, M. Hervieu and J. Hejtmanek, *Appl. Phys. A*, in press.
19 J. Hejtmanek, Z. Jirak, M. Marysko, C. Martin, A. Maignan, M. Hervieu and B. Raveau, *Phys. Rev. B*, 1999, **60**, 14057.
20 C. Autret, C. Martin, A. Maignan, M. Hervieu, B. Raveau, G. André, F. Bourée, A. Kurbakov and V. Trounov, *J. Magn. Magn. Mater.*, in press.
21 C. Martin, A. Maignan, M. Hervieu, B. Raveau, Z. Jirak, A. Kurbakov, V. Trounov, G. André and F. Bourée, *J. Magn. Magn. Mater.*, 1999, **205**, 184.
22 M. Hervieu, C. Martin, A. Maignan, G. Van Tendeloo, Z. Jirak, J. Hejtmanek, A. Barnabé, D. Thopart and B. Raveau, *Chem. Mater.*, 2000, **12**, 1456.
23 C. Martin, A. Maignan, M. Hervieu and B. Raveau, *Phys. Rev. B*, 1999, **60**, 12191.
24 R. D. Shannon, *Acta. Crystallogr., Sect. A*, 1976, **A32**, 751.
25 P. M. Woodward, T. Vogt, D. E. Cox, A. A. Arulraj, C. N. Rao, P. Karen and A. K. Cheetham, *Chem. Mater.*, 1998, **10**, 3652.
26 L. M. Rodriguez-Martinez and J. P. Attfield, *Phys. Rev. B*, 1996, **54**, R15622; L. M. Rodriguez-Martinez and J. P. Attfield, *Phys. Rev. B*, 1998, **58**, 2426.
27 S. Shinomura, T. Tonegawa, K. Tajima, N. Wakabayashi, N. Ikeda, T. Shobu, Y. Noda, Y. Tomioka and Y. Tokura, *Phys. Rev. B*, 2000, **62**, 3875.